Multimodality Imaging to Assess Immediate Response to Irreversible Electroporation in a Rat Liver Tumor Model[1]

Yue Zhang, MS
Sarah B. White, MD
Jodi R. Nicolai, MS
Zhuoli Zhang, MD, PhD
Derek L. West, MD
Dong-hyun Kim, PhD
A. Lee Goodwin, BS
Frank H. Miller, MD
Reed A. Omary, MD, MS[2]
Andrew C. Larson, PhD

Purpose: To compare changes on ultrasonographic (US), computed tomographic (CT), and magnetic resonance (MR) images after irreversible electroporation (IRE) ablation of liver and tumor tissues in a rodent hepatoma model.

Materials and Methods: Studies received approval from the institutional animal care and use committee. Forty-eight rats were used, and N1-S1 tumors were implanted in 24. Rats were divided into groups and allocated for studies with each modality. Imaging was performed in normal liver tissues and tumors before and after IRE. MR imaging was performed in one group before and after IRE after hepatic vessel ligation. US images were graded to determine echogenicity changes, CT attenuation was measured (in Hounsfield units), and MR imaging signal-to-noise ratio (SNR) was measured before and after IRE. Student *t* test was used to compare attenuation and SNR measurements before and after IRE ($P < .05$ indicated a significant difference).

Results: IRE ablation produced greater alterations to echogenicity in normal tissues than in tumors. Attenuation in ablated liver tissues was reduced compared with that in control tissues ($P < .001$), while small attenuation differences between ablated (42.11 HU ± 2.11) and control (45.14 HU ± 2.64) tumors trended toward significance ($P = .052$). SNR in ablated normal tissues was significantly altered after IRE (T1-weighted images: pre-IRE, 145.95 ± 24.32; post-IRE, 97.80 ± 18.03; $P = .004$; T2-weighted images, pre-IRE, 47.37 ± 18.31; post-IRE, 90.88 ± 37.15; $P = .023$). In tumors, SNR differences before and after IRE were not significant. No post-IRE signal changes were observed after hepatic vessel ligation.

Conclusion: IRE induces rapid changes on gray-scale US, unenhanced CT, and MR images. These changes are readily visible and may assist a performing physician to delineate ablation zones from the unablated surrounding parenchyma.

Online supplemental material is available for this article.

[1] From the Department of Bioengineering, University of Illinois at Chicago, Chicago, Ill (Y.Z., A.C.L.); Department of Radiology (Y.Z., S.B.W., J.R.N., Z.Z., D.L.W., D.H.K., A.L.G., F.H.M., R.A.O., A.C.L.) and Robert H. Lurie Comprehensive Cancer Center (A.C.L.), Northwestern University, 737 N Michigan Ave, Suite 1600, Chicago, IL 60611; Department of Radiology, Medical College of Wisconsin, Milwaukee, Wis (S.B.W.); and Department of Biomedical Engineering, Northwestern University, Evanston, Ill (A.C.L.). Received April 29, 2013; revision requested July 2; revision received October 9; accepted November 5; final version accepted December 9. Supported by the Allied Scientist Grant from the Society of Interventional Radiology Foundation. **Address correspondence to** A.C.L. (e-mail: *a-larson@northwestern.edu*).

[2] **Current address:** Department of Radiology and Radiological Sciences, Vanderbilt University, Nashville, Tenn.

Irreversible electroporation (IRE) has been studied as a tissue ablation modality (1,2). Permanent nanoscale pores are created with application of strong short-lived electrical fields across cell membranes; this leads to a loss of homeostasis and eventual cell death (3). IRE offers several potential advantages over thermal ablation approaches (4,5), specifically, a relatively short ablation procedure and the ability to ablate adjacent large blood vessels (6–8); thus, IRE may be well suited for ablation of solid organ tumors, such as primary or metastatic lesions in the liver. In preclinical settings, IRE was shown to be effective for targeted ablation of liver tumors in an N1-S1 rat model (9) and a VX2 rabbit model (10).

During ablation procedures, imaging is used to locate targeted lesions (11–13), monitor tissue ablation (14–16), and evaluate treatment effectiveness (17–19). Because of its ease of use and broad availability, ultrasonography (US) is most routinely used during ablation procedures in clinical settings (20–22). Computed tomography (CT) has been used for tumor targeting and in outcome evaluation after IRE ablation procedures (23,24). Magnetic resonance (MR) imaging can be useful for tumor targeting and in the assessment of immediate response after IRE (25–27). Echogenecity changes are observed during US of normal liver tissues after IRE ablation (28,29); both CT and MR imaging have been used to characterize tumors 24 hours after IRE (9,10).

During this preclinical study, we performed IRE procedures in both normal liver tissue and hepatic tumors. The purpose of the study was to compare induced changes on US, CT, and MR images shortly after IRE ablation of both normal liver parenchyma and hepatic tumors in a rodent hepatic carcinoma model.

Advance in Knowledge

- Multimodality imaging potentially can be used to immediately depict irreversible electroporation (IRE) ablation zones within targeted liver tissues.

Implication for Patient Care

- US, CT, and MR imaging potentially can be used intraprocedurally to optimize IRE to ensure successful and effective ablation of targeted lesions.

Materials and Methods

Experimental Overview

In vivo IRE procedures were performed in both normal liver parenchyma and hepatic tumors. Imaging (US, CT, and MR imaging) was performed before and immediately after application of IRE pulses. On delivery, the 48 animals were randomly divided into eight groups (six rats per group): US was performed in two groups (US_N, normal tissue ablation; US_T, tumor ablation), CT was performed in three groups (CT_N, normal tissue ablation; CT_T, tumor ablation; CT_C, control tumor without ablation), and MR imaging was performed in three groups (MR_N, normal tissue ablation; MR_T, tumor ablation; MR_L, hepatic vessels ligated prior to IRE). In the US_N, US_T, MR_N, and MR_T groups, each rat underwent IRE procedures and survived for 24 hours to allow for definitive formation of IRE-induced necrotic tissue regions (1,30). Rats in the CT_N or CT_T group were euthanized 30 minutes after IRE for follow-up CT. CT of live rats was not possible given the institutional restrictions regarding use of CT instrumentation; this limitation necessitated the inclusion of a control group (CT_C) to obtain baseline CT measurements in tumors and normal liver parenchyma given that baseline and post-IRE CT was not possible in the same animals. CT was performed in the CT_C rats without IRE. Rats in the MR_L group underwent pre- and post-IRE MR imaging, with IRE performed immediately after portal vein and hepatic artery ligation to investigate the effect of perfusion on IRE-induced signal changes.

Animal Model

Experiments were approved by the institutional animal care and use committee of Northwestern University. The 48 male Sprague-Dawley rats (weight range, 300–350 g) used for these experiments were randomly assigned to a group. Twenty-four of the animals were divided among four groups: US_T, CT_T, CT_C, and MR_T. A total of 5×10^6 N1-S1 cells (CRL-1603; American Type Culture Collection, Manassas, Va) were implanted in the left lateral lobe of each rat after median laparotomy, and 7–10 days were allowed for tumor growth prior to IRE.

IRE Procedures

After pre-IRE imaging, rats from MR groups were removed from the imager. Rats from all groups were kept in the supine position during the subsequent IRE procedures and during the follow-up postprocedural imaging studies. The left lateral lobe of the liver was exposed after median laparotomy. For normal hepatic parenchyma ablation (US_N, CT_N, MR_N, and MR_L groups), two parallel

Published online before print
10.1148/radiol.14130989 **Content code:** GI

Radiology 2014; 271:721–729

Abbreviations:
GRE = gradient echo
IRE = irreversible electroporation
SNR = signal-to-noise ratio

Author contributions:
Guarantor of integrity of entire study, A.C.L.; study concepts/study design or data acquisition or data analysis/interpretation, all authors; manuscript drafting or manuscript revision for important intellectual content, all authors; approval of final version of submitted manuscript, all authors; literature research, Y.Z., Z.Z., D.L.W., D.H.K., A.L.G.; experimental studies, Y.Z., S.B.W., J.R.N., Z.Z., D.L.W., D.H.K., A.L.G., R.A.O., A.C.L.; statistical analysis, Y.Z., Z.Z., D.L.W., A.L.G.; and manuscript editing, Y.Z., S.B.W., Z.Z., D.L.W., A.L.G., F.H.M., R.A.O., A.C.L.

Funding:
This research was supported by the National Institutes of Health (grants R01 CA 141047 and R01 CA 159178) and a Cancer Center Support Grant (NCI CA060553).

Conflicts of interest are listed at the end of this article.

needle electrodes with 1-cm spacing were inserted into the center of the left lateral lobe. For tumor ablation (US_T, CT_T, and MR_T groups), tumors were located visually and were palpated digitally between the thumb and forefinger to approximate the configuration of the tumor mass. Next, needle electrodes were positioned such that the needles were aligned along the axis of the largest tumor dimension. A 1-cm electrode separation was maintained, as the needles had previously been secured in a 15-mm-thick plastic spacing block. Next, the electrodes were connected to the IRE generator (ECM830; Harvard Apparatus, Holliston, Mass) such that 2500-V square wave pulses were applied to the two parallel electrodes with the following protocol: number of pulses, eight; duration of each pulse, 100 μsec; and interval between pulses, 100 msec (9,25). After IRE, the electrodes were disconnected. The IRE procedures were performed by one author (Y.Z., 5 years of experience). For all modalities, post-IRE imaging was performed 30 minutes after the ablation procedures.

US Studies

For US studies, imaging was performed by using a 12-MHz transducer US probe (M7; MindRay, Shenzhen, China) placed on the exposed liver, with an acoustic window created with US gel. In the US_N group, US was performed to examine normal hepatic parenchyma; in the US_T group, US was performed to examine the tumor. Thirty minutes after IRE, US was repeated to acquire post-IRE images. Two certified attending interventional radiologists (S.B.W., D.L.W.; 3 and 9 years of experience, respectively) performed the US procedures. Selected focal zone depth, gain, and tissue harmonic settings were individually optimized by the operator (S.B.W. or D.L.W.) on a case-by-case basis during acquisition of the initial pre-IRE images, and these parameters were unchanged during acquisition of post-IRE images.

CT Studies

Unenhanced CT was performed (A.L.G., 28 years experience) in CT_N, CT_T, and CT_C groups by using a 64-section helical clinical system (Sensation; Siemens Healthcare, Malvern, Pa). For animals in the CT_N and CT_T groups, rats were euthanized 30 minutes after IRE for follow-up CT; CT was performed in CT_C rats without IRE. The CT parameters were 120 kVp and 250 mA, with images reconstructed by using a 1-mm section thickness.

MR Imaging

MR imaging was performed (Y.Z., 5 years experience) in the MR_N, MR_T, and MR_L groups by using a 7-T animal imager (ClinScan; Bruker BioSpin, Ettlingen, Germany). Pre- and post-IRE MR imaging was performed by using T1-weighted gradient-echo (GRE) and T2-weighted fast spin-echo sequences. The general parameters for these sequences were as follows: section thickness, 1 mm; field of view, 64 × 128 mm; matrix, 96 × 192; and bandwidth, 500 Hz/pixel. For the T1-weighted sequence, the specific parameters were as follows: repetition time msec/echo time msec, 200/2.68; flip angle, 90°; and six averages acquired. For the T2-weighted sequence, the specific parameters were as follows: ≈2634/44.1; flip angle, 180°; and three averages acquired. To reduce motion artifacts, a small-animal monitoring and gating system (SA Instruments, Stony Brook, NY) was used during the acquisition of T2-weighted fast spin-echo images.

Histologic Evaluation

Rats in the CT_N and CT_T groups were euthanized 30 minutes after IRE. Rats in the MR_L group were euthanized 30 minutes after post-IRE imaging. Rats in the CT_C group were euthanized without undergoing IRE. Animals in the US_N, US_T, MR_N, and MR_T groups were euthanized 24 hours after IRE. At necropsy, livers were harvested and fixed in 10% buffered formaldehyde solution, sliced at 3-mm intervals, and embedded in paraffin. Liver samples were cut in 4-μm-thick slices and stained with hematoxylin-eosin. Histologic slides were digitized with an optical magnification image acquisition system (TissueGnostics Cell Analyzer; TissueGnostics, Vienna, Austria) that permitted examination of entire slides with a low magnification (×10), as well as examination of regional details at a higher magnification (×40) (Zeiss Axioskop upright fluorescence microscope with CRi NUANCE spectral camera; Carl Zeiss, Jena, Germany).

In control rats and those that underwent IRE procedures, separate samples from normal hepatic parenchyma and tumor tissues were collected at necropsy and prepared for transmission electron microscopy. The post-IRE samples were obtained in rats euthanized 30 minutes after post-IRE imaging. These tissue samples were sliced into 1-mm cubes and placed in Karnovsky fixative for 2 weeks to preserve structures. Samples were then stained with osmium tetraoxide (OsO_4), dehydrated, and embedded in resin. Samples were then sliced with an ultramicrotome to a thickness of 70 nm for transmission electronic microscopy (FEI Tecnai Spirit G2; FEI, Hillsboro, Ore).

Data Analysis

ImageJ software package (National Institutes of Health, Bethesda, Md) was used for image analysis. Pre- and post-IRE US images were individually reviewed by two radiologists (S.B.W., D.L.W.) to determine echogenicity prior to and immediately after IRE by using a four-point grading scale: 0 indicated no change; 1, slight change; 2, clear change; and 3, dramatic change (only the tumor echogenicity change was considered for scoring in the US_T group). Images with discordant scores were reviewed by a third radiologist (Z.Z., more than 10 years experience in diagnostic radiology). CT images initially were reviewed with a window level and width of 50 and 150 HU, respectively. To improve subjective conspicuity of the findings, the observer was free to adjust the window width and level at will. Regions of interest were drawn to measure attenuation in different regions; these regions were the normal liver after IRE and the adjacent untreated normal liver in the CT_N group, the tumor region after IRE in the CT_T

group, and the tumor region without IRE in the CT_C group. On pre- and post-IRE T1- and T2-weighted MR images, signal-to-noise ratio (SNR) was measured in both the MR_N and MR_T groups.

Statistical Analysis

Independent *t* tests were used to compare CT attenuation measurements obtained before and after IRE. Paired *t* tests were performed to compare SNR measurements from pre- and post-IRE T1- and T2-weighted images. These analyses were performed with a software package (SPSS, version 12; SPSS, Chicago, Ill), with *P* values less than .05 considered to indicate a significant difference.

Results

Multimodality Imaging

Multimodality imaging of IRE in liver parenchyma.—On US images, ablated tissues appeared as a hypoechoic region adjacent to the IRE probes, and in most cases, a hyperechoic (when compared with normal surrounding hepatic parenchyma) rim also was seen (Fig 1, *A* and *B*). On CT images, ablated normal tissues appeared as hypoattenuating foci when compared with surrounding unablated tissues (Fig 1, *C* and *D*). Representative MR images obtained in the normal liver prior to and immediately after IRE are also shown. IRE-affected tissues were clearly demarcated from surrounding normal hepatic parenchyma; electroporated tissues were hypointense on T1-weighted images (Fig 1, *F*) but were consistently hyperintense on T2-weighted images (Fig 1, *H*).

Multimodality imaging of IRE in liver tumors.—Tumors appeared heteroechoic (hyperechoic peripherally and isoechoic centrally) on pre-IRE US images (Fig 2, *A*). On post-IRE US images (Fig 2, *B*), all tissues adjacent to the IRE probe (both normal parenchyma and tumor) became more hypoechoic, and a hyperechoic rim developed along the periphery of the ablation zone; the site of the electrodes was also noted and appeared as a linear focus of hyperechogenicity due to air introduced during initial probe placement. On CT images, control tumors appeared as hypoattenuating foci (Fig 2, *C*); after tumor IRE, a large hypoattenuating focus appeared, and the tumor margin could no longer be seen clearly (Fig 2, *D*). Representative MR images from tumor ablation procedures before and after IRE are shown. Pre-IRE tumors appeared hypointense on T1-weighted images (Fig 2, *E*) and hyperintense on T2-weighted images (Fig 2, *G*). After IRE, a large hypointense region was observed corresponding to the ablated tissue zones within T1-weighted images (Fig 2, *F*). After IRE, a hyperintense region of ablated normal tissues appeared surrounding the central hyperintense tumor on T2-weighted images (Fig 2, *H*).

Hepatic Ligation

In the animals that underwent portal vein and hepatic artery ligation prior to MR imaging–monitored IRE procedures, no post-IRE–induced signal changes were observed; representative images for one animal in this group are shown in Figure E1 (online).

Histologic Evaluation

Within hemotoxylin-eosin slides from tissues collected 30 minutes after IRE (Fig E2, *A* [online]), ablated zones within normal hepatic parenchyma were pale relative to adjacent nonablated tissue regions, indicating degeneration of eosinophilic structures (cytoplasm and extracellular spaces); however, nuclei structure was maintained at this early follow-up interval. At 24 hours after IRE (Fig E2, *B* and *E* [online]), ablated regions were increasingly pale compared with peripheral nonablated liver tissues. At this follow-up interval, some of the nuclei decreased in size, indicating presence of coagulation necrosis; furthermore, an influx of red blood cells was observed in the extracellular spaces (Fig E2, *E*). For hemotoxylin-eosin–stained tumor specimens, ablation zones were observed to encompass the entire tumor within samples collected both immediately after IRE (Fig 3, *C* and *D*) and 24 hours after IRE (Fig 3, *E* and *F*). Tumor cell nuclei agglutinations were observed 30 minutes after IRE. Tumor cells became more loosely arranged within the specimens collected 24 hours after IRE compared with tumor cells collected prior to IRE procedures. The nuclear cytoplasm ratio for these tumor cells tended to increase 24 hours after IRE.

When transmission electron microscopy images of untreated tumor cells (Fig E4, *A* and *B* [online]) were compared with images of normal hepatocytes (Fig E3, *A* and *B* [online]), the untreated tumor cells had a larger nucleus. Thirty minutes after IRE, *(a)* small pores appeared within the nuclear membrane; *(b)* a completely intact cell membrane was no longer observed; *(c)* chromatin condensation was observed, with chromatin abutted to the nuclear membrane; and *(d)* most organelles maintained their structures, although some vacuoles were present (Fig E4, *C* and *D* [online]). At 24 hours after IRE, small pores could still be seen along the nuclear membrane, and the basal layer was thinner compared with tissue samples obtained immediately after IRE. Electron density of the nucleus decreased 24 hours after IRE relative to the sample collected immediately after ablation, indicating degeneration, migration, or both, of the chromatin. Most organelles lost their structure, and more vacuolar degenerations were noted in the cytoplasm (Fig E4, *E* and *F* [online]). Similar changes were observed on transmission electron microscopy images of both normal and tumor tissues, with the primary difference being the smaller size of the cell nucleus and the larger nuclear cytoplasm ratio.

Statistical Analysis

For US images, the average grade for echogenicity change was 2.0 for the ablated liver and 1.3 for ablated tumor tissues. For CT, attenuation in the ablated liver (62.53 HU ± 2.24) was significantly different ($P < .001$) from that in the unablated normal parenchyma (46.99 HU ± 5.259). While small, the attenuation difference between the

Figure 1

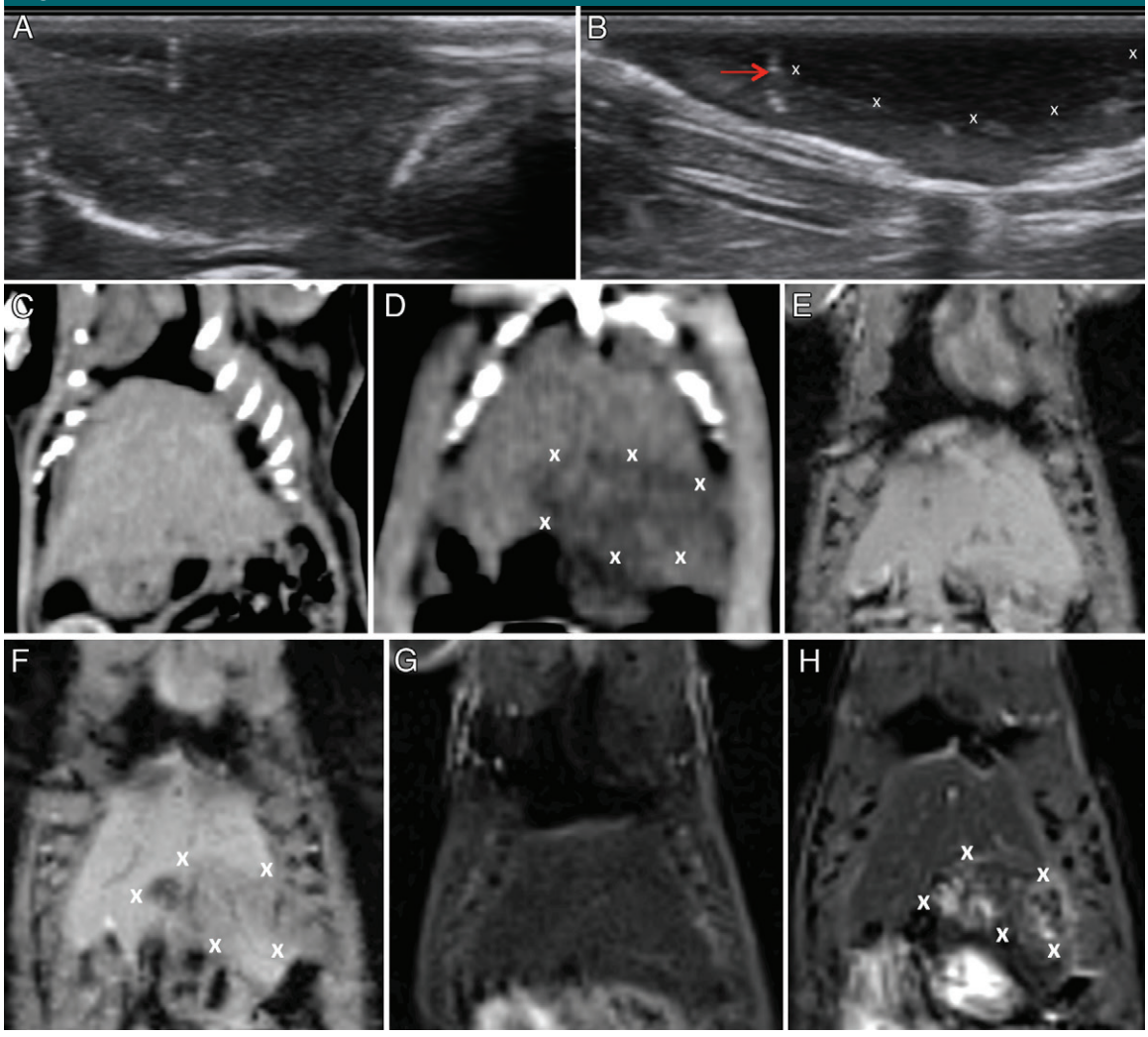

Figure 1: Representative images acquired before and after IRE in normal hepatic parenchyma. *A*, Pre-IRE US image shows normal liver parenchyma. *B*, Post-IRE US image shows a hypoechoic region *(X)* in the liver parenchyma and represents the ablation zone. Arrow = IRE probe position (hyperechogenicity related to introduction of air at probe placement). *C*, Pre-IRE CT image shows normal liver parenchyma. *D*, Post-IRE CT image shows ablation zones as areas of hypoattenuation *(X)*. *E*, Pre-IRE T1-weighted MR image shows normal liver parenchyma. *F*, T1-weighted MR image shows ablation zone as a hypointense region *(X)*. *G*, Pre-IRE T2-weighted MR image shows normal liver parenchyma. *H*, T2-weighted MR image shows ablation zone as a hyperintense region *(X)*.

ablated tumor (42.11 HU ± 2.11) and the control tumor (45.14 HU ± 2.64) trended toward significance (P = .052). For MR images, SNR measurements in the ablated normal liver were significantly increased after IRE (T1-weighted: pre-IRE, 145.95 ± 24.32; post-IRE, 97.80 ± 18.03; P = .004; T2-weighted: pre-IRE, 47.37 ± 18.31; post-IRE, 90.88 ± 37.15; P = .023). The SNR difference between tumors before and after IRE was not significant (pre-IRE, 102.13 ± 31.36; post-IRE, 101.09 ± 21.66; P = .940).

Discussion

IRE is a potentially highly effective tissue ablation technique. Imaging-based intraprocedural or early postprocedural monitoring approaches may be crucial to optimize IRE procedures. Our experiments successfully showed that IRE induces rapid changes apparent on US, CT, and MR images during normal hepatic tissue ablation and during tumor ablation (significant changes occur in the normal liver tissue surrounding the tumors). Immediately after IRE procedures, the early alterations on gray-scale US, unenhanced CT, and MR images are markedly greater in normal liver parenchyma than in ablated tumor tissues.

Our US findings in normal hepatic parenchyma after IRE were similar to those in previous studies (23,28), which

Figure 2

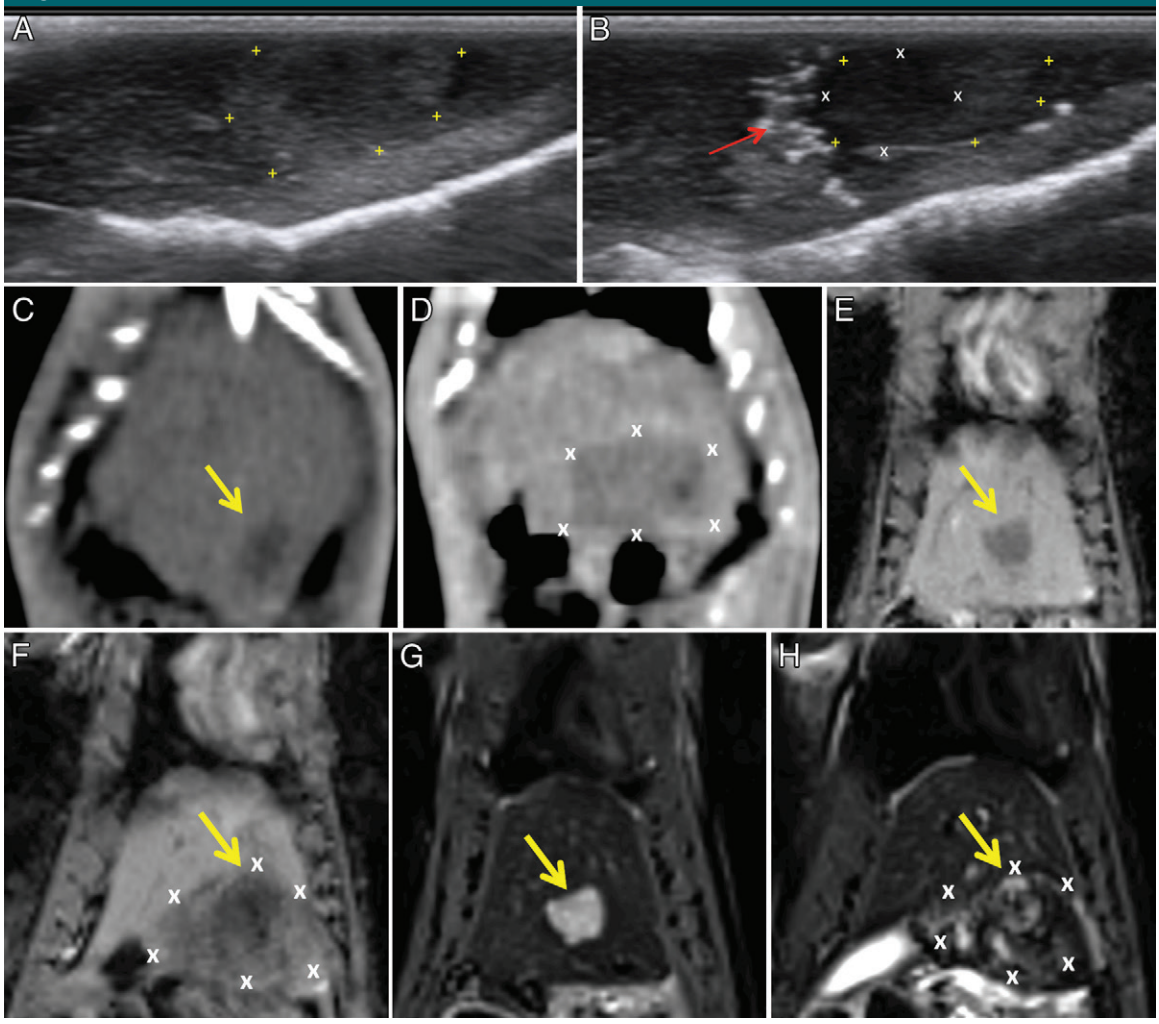

Figure 2: Representative images acquired before and after IRE in tumor tissues. *A*, Pre-IRE US image shows the tumor *(+)* appeared hyperechoic peripherally and isoechoic centrally when compared with normal hepatic parenchyma. *B*, Post-IRE US image shows normal and tumor tissues adjacent to the IRE probe *(X)* become hypoechoic. Arrow = probe position. *C*, CT image shows control tumor (arrow) as a hypoattenuating focus. *D*, Post-IRE CT image shows the ablation zone *(X)* as an area of hypoattenuation; a clear tumor boundary is difficult to determine. *E*, Pre-IRE T1-weighted MR image shows a hypointense tumor (arrow). *F*, Post-IRE T1-weighted MR image shows the ablation zone as a hypointense region *(X)* encompassing the tumor (arrow). *G*, Pre-IRE T2-weighted MR image shows hyperintense tumor (arrow). *H*, Post-IRE T2-weighted MR image shows a heterogeneously hyperintense region *(X)* encompassing a central hyperintense tumor (arrow).

showed that ablated tissues appear as a hypoechoic focus. For tumor ablation, both normal and tumor tissues adjacent to the IRE probe became more hypoechoic within post-IRE US images. The results of these echogenicity grading scale studies provide additional evidence that it would be feasible to use intraprocedural US to monitor IRE.

During CT studies, IRE induced a large focus of attenuation within both normal and tumor tissues after ablation (IRE-induced hypoattenuation on CT images). Because the tumor initially appears as a focus of hypoattenuation, the tumor margin is no longer clearly seen on post-IRE CT images. Quantitative measurements enabled us to confirm that attenuation decreases were significantly greater in normal tissues than in tumor tissues after ablation. Nonetheless, the dramatic image contrast effects observed on post-IRE CT images (along with the relatively rapid imaging time compared with MR imaging), suggest that this imaging modality may be ideal for intraprocedural or immediate postprocedural monitoring. At this early stage (30 minutes after IRE), only the focus of hypoattenuation was observed without any hyperattenuating peripheral rim. This finding is in contrast to the finding of a prior

Figure 3

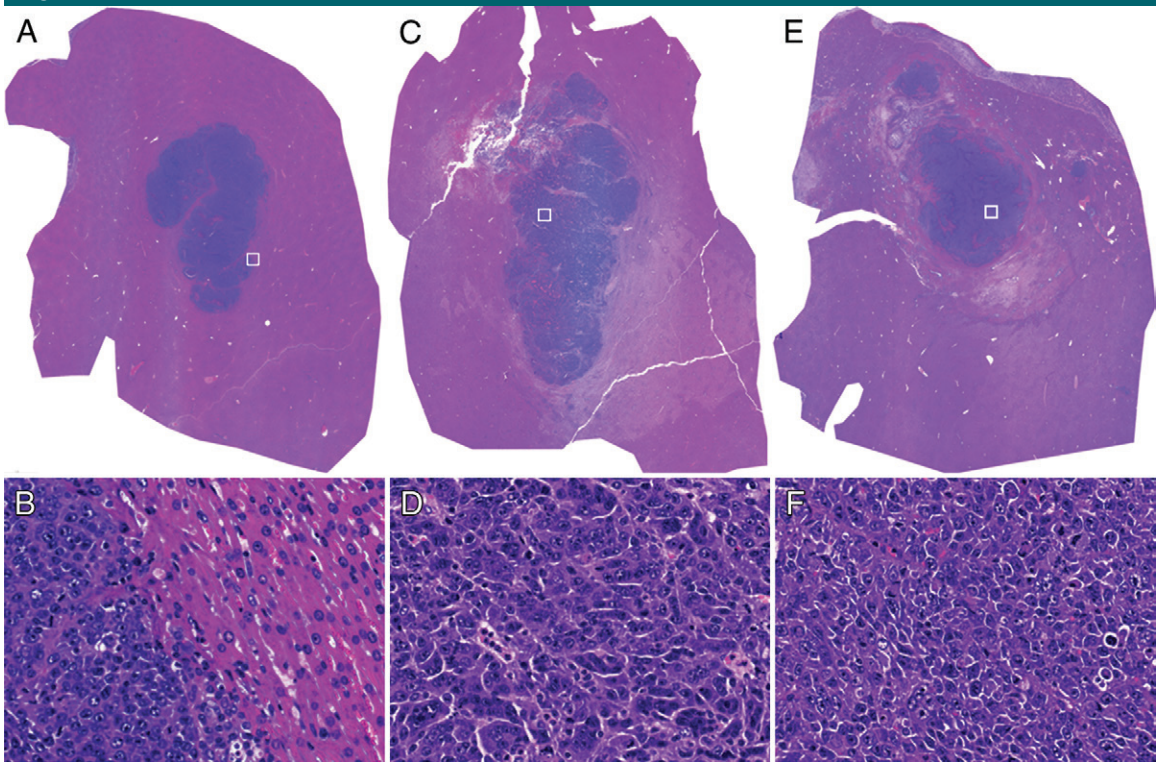

Figure 3: Representative hematoxylin-eosin–stained histologic slides from tumor tissues in, *A*, *B*, control rats, *C*, *D*, rats sacrificed 30 minutes after IRE, and *E*, *F*, rats sacrificed 24 hours after IRE. Nucleus agglutinations can be observed 30 minutes after IRE. Tumor cells are arranged more loosely in *F* than in *B*. The nucleus-to-cytoplasm ratio tended to increase 24 hours after IRE. □ = approximate locations for *D*, *E*, and *F*. Original magnifications are ×10 for *A*, *B*, and *C* and ×40 for *D*, *E*, and *F*.

CT study, in which the researchers described the appearance of a hyperattenuating rim after IRE; however, this prior finding was observed 2 days after IRE in a normal liver parenchyma ablation study in which both unenhanced CT and contrast material–enhanced CT were used (23).

On post-IRE CT images and T1- and T2-weighted MR images, there was a well-demarcated boundary between the ablation zone and the surrounding normal tissues. On post-IRE US images, although a hypoechoic region could be observed, boundaries between ablated tissues and surrounding tissue were difficult to visualize. One reason for this finding may have been that we were unable to capture the entire ablation zone since our US transducer could only be applied to a limited area because of the small size of the rat liver. We expect this limitation would be overcome in a clinical setting or a large-animal model.

MR findings after hepatic ligation enabled us to confirm our assumption from a previous study (25) about MR signal alteration due to IRE in normal hepatic parenchyma, indicating that early signal changes are likely the result of local fluid accumulation owing to transient permeabilization of blood vessels, with subsequent fluid build-up after rapid extravasation into the treated tissue zones. This finding may also explain why MR signal changes are much larger in normal tissues after IRE. The phenomenon of local fluid accumulation is very apparent in normal tissue, since the liver is a well-vascularized organ with large blood volume. In contrast, N1-S1 hepatic carcinoma leads to hypovascular tumors with relatively heterogeneous vascularization. The latter characteristics could conceivably result in a reduction to the local volume of fluid extravasated after IRE within tumor tissues and a more heterogeneous extravasation pattern than that observed in normal tissues. All measurements (US, CT, and MR imaging) indicated that IRE introduces more dramatic signal changes in normal tissues and that these alterations can be detected readily with each conventional imaging modality. Another factor that could contribute to these significant differences between tumor and normal liver tissues could be the marked dilation of the hepatic sinusoidal spaces (28), an effect that was not observed in the tumor tissues.

Our findings with IRE are similar to those found with other ablation technologies. Both radiofrequency ablation and microwave ablation appear as foci of hypoattenuation on CT images (31) and are hyperechoic on US images (32)

due to release of gas during tissue heating. Both radiofrequency ablation and microwave ablation have decreased T2-weighted signal intensity (33), increased T1-weighted signal intensity, and show no enhancement after administration of a gadolinium chelate (34). Cryoablation is more easily seen with all imaging modalities because of the formation of an ice ball that is hypoattenuated compared with the surrounding liver at CT (35,36). On MR images, the iceball appears hypointense on T2-weighted images, and once the ice ball melts, the ablation defect appears hyperintense on T2-weighted images (37).

One limitation of this study was the lack of serial monitoring after IRE. However, the singular focus of this current multimodality study was immediate post-IRE imaging. Early imaging may be important to inform practitioners about the position and extent of induced IRE ablation zones; ultimately, it will be critical to determine whether the induced ablation zone completely covers the tumor volume or whether further ablation is necessary. However, recent studies have shown that IRE-induced tissue damage can evolve dramatically even in the first 100 minutes after the procedure (28). Additional future studies will be important to correlate early postprocedural imaging findings with delayed measurements days to weeks after IRE. Finally, given that the anatomic imaging approaches described in this study likely depict tertiary fluid accumulation rather than direct effects on cell membrane integrity, additional development of functional imaging methods sensitive to membrane permeability ultimately may be warranted. Such methods potentially could be used to probe endogenous contrast mechanisms (water mobility alterations) or use exogenous tracers wherein cellular uptake, activation state, or both, are altered via IRE ablation.

Relatively recent studies have shown that viable tumor cells adherent to the electrodes after radiofrequency ablation (38) may serve as an independent predictor of local tumor progression (39–41). For these methods, tumor cell viability can be evaluated rigorously by using markers of mitochondrial activity (40,42) or proliferation (Ki-67) (39). Similar assays might also prove useful to augment intraprocedural or follow-up cross-sectional imaging measurements to more accurately predict longitudinal responses after IRE ablation procedures. Although we did not study contrast-enhanced MR, CT, or US in the current investigation, contrast agents may prove valuable in the assessment of tissue responses after IRE. Electroporation clearly affects microvessel wall and cell membrane permeability and thus alters contrast agent kinetics (43); imaging for the quantification of transient or permanent alterations to these kinetics could serve as an additional biomarker of IRE response.

In conclusion, IRE induces rapid changes that can be observed readily on US, MR, and CT images. However, signal changes on gray-scale US, unenhanced CT, and T1- and T2-weighted MR images were significantly greater within normal tissues than within tumor tissues after IRE ablation procedures. This study enabled us to confirm the feasibility of using these modalities in real time to monitor ablation intraprocedurally. MR imaging findings after hepatic ligation suggest that early signal changes after IRE are the result of local fluid accumulation in the treated tissue zones. Future studies are necessary to develop superior imaging methods with which to better characterize electroporation-induced changes within tumor tissues to ensure accurate predictions of response.

Practical application: We have shown that conventional imaging modalities (gray-scale US, unenhanced CT, and T1- and T2-weighted MR imaging) can be used to immediately depict IRE ablation zones within normal hepatic parenchyma.

Acknowledgment: This work was supported by the Northwestern University Mouse Histology and Phenotyping Laboratory.

Disclosures of Conflicts of Interest: Y.Z. No relevant conflicts of interest to disclose. **S.B.W.** No relevant conflicts of interest to disclose. **J.R.N.** No relevant conflicts of interest to disclose. **Z.Z.** No relevant conflicts of interest to disclose. **D.L.W.** No relevant conflicts of interest to disclose. **D.H.K.** No relevant conflicts of interest to disclose. **A.L.G.** No relevant conflicts of interest to disclose. **F.H.M.** No relevant conflicts of interest to disclose. **R.A.O.** No relevant conflicts of interest to disclose. **A.C.L.** No relevant conflicts of interest to disclose.

References

1. Rubinsky B, Onik G, Mikus P. Irreversible electroporation: a new ablation modality—clinical implications. Technol Cancer Res Treat 2007;6(1):37–48.
2. Lee EW, Loh CT, Kee ST. Imaging guided percutaneous irreversible electroporation: ultrasound and immunohistological correlation. Technol Cancer Res Treat 2007;6(4):287–294.
3. Edd JF, Horowitz L, Davalos RV, Mir LM, Rubinsky B. In vivo results of a new focal tissue ablation technique: irreversible electroporation. IEEE Trans Biomed Eng 2006;53(7):1409–1415.
4. Ahmed M, Goldberg SN. Thermal ablation therapy for hepatocellular carcinoma. J Vasc Interv Radiol 2002;13(9 Pt 2):S231–S244.
5. Boaz TL, Lewin JS, Chung YC, Duerk JL, Clampitt ME, Haaga JR. MR monitoring of MR-guided radiofrequency thermal ablation of normal liver in an animal model. J Magn Reson Imaging 1998;8(1):64–69.
6. Kingham TP, Karkar AM, D'Angelica MI, et al. Ablation of perivascular hepatic malignant tumors with irreversible electroporation. J Am Coll Surg 2012;215(3):379–387.
7. Lee YJ, Lu DS, Osuagwu F, Lassman C. Irreversible electroporation in porcine liver: short- and long-term effect on the hepatic veins and adjacent tissue by CT with pathological correlation. Invest Radiol 2012;47(11):671–675.
8. Maor E, Ivorra A, Leor J, Rubinsky B. The effect of irreversible electroporation on blood vessels. Technol Cancer Res Treat 2007;6(4):307–312.
9. Guo Y, Zhang Y, Klein R, et al. Irreversible electroporation therapy in the liver: longitudinal efficacy studies in a rat model of hepatocellular carcinoma. Cancer Res 2010;70(4):1555–1563.
10. Lee EW, Wong D, Tafti BA, et al. Irreversible electroporation in eradication of rabbit VX2 liver tumor. J Vasc Interv Radiol 2012;23(6):833–840.
11. Sugiura N, Takara K, Ohto M, Okuda K, Hirooka N. Percutaneous intratumoral injection of ethanol under ultrasound imaging for treatment of small hepatocellular carcinoma. Acta Hepatol Jpn 1983;24:920–923.

12. Deng J, Virmani S, Yang GY, et al. Intraprocedural diffusion-weighted PROPELLER MRI to guide percutaneous biopsy needle placement within rabbit VX2 liver tumors. J Magn Reson Imaging 2009;30(2):366–373.

13. Brandt KR, Charboneau JW, Stephens DH, Welch TJ, Goellner JR. CT- and US-guided biopsy of the pancreas. Radiology 1993;187(1):99–104.

14. Gilbert JC, Onik GM, Hoddick WK, Rubinsky B. Real time ultrasonic monitoring of hepatic cryosurgery. Cryobiology 1985;22(4):319–330.

15. Nour SG, Goldberg SN, Wacker FK, et al. MR monitoring of NaCl-enhanced radiofrequency ablations: observations on low- and high-field-strength MR images with pathologic correlation. Radiology 2010;254(2):449–459.

16. Holbrook AB, Santos JM, Kaye E, Rieke V, Pauly KB. Real-time MR thermometry for monitoring HIFU ablations of the liver. Magn Reson Med 2010;63(2):365–373.

17. Mikami S, Tateishi R, Akahane M, et al. Computed tomography follow-up for the detection of hepatocellular carcinoma recurrence after initial radiofrequency ablation: a single-center experience. J Vasc Interv Radiol 2012;23(10):1269–1275.

18. Krause BJ, Herrmann K, Wieder H, zum Büschenfelde CM. 18F-FDG PET and 18F-FDG PET/CT for assessing response to therapy in esophageal cancer. J Nucl Med 2009;50(Suppl 1):89S–96S.

19. Okuma T, Matsuoka T, Okamura T, et al. 18F-FDG small-animal PET for monitoring the therapeutic effect of CT-guided radiofrequency ablation on implanted VX2 lung tumors in rabbits. J Nucl Med 2006;47(8):1351–1358.

20. Solbiati L, Giangrande A, De Pra L, Bellotti E, Cantù P, Ravetto C. Percutaneous ethanol injection of parathyroid tumors under US guidance: treatment for secondary hyperparathyroidism. Radiology 1985;155(3):607–610.

21. Minami Y, Kudo M. Review of dynamic contrast-enhanced ultrasound guidance in ablation therapy for hepatocellular carcinoma. World J Gastroenterol 2011;17(45):4952–4959.

22. Solbiati L, Ierace T, Goldberg SN, et al. Percutaneous US-guided radio-frequency tissue ablation of liver metastases: treatment and follow-up in 16 patients. Radiology 1997;202(1):195–203.

23. Lee EW, Chen C, Prieto VE, Dry SM, Loh CT, Kee ST. Advanced hepatic ablation technique for creating complete cell death: irreversible electroporation. Radiology 2010;255(2):426–433.

24. Thomson KR, Cheung W, Ellis SJ, et al. Investigation of the safety of irreversible electroporation in humans. J Vasc Interv Radiol 2011;22(5):611–621.

25. Zhang Y, Guo Y, Ragin AB, et al. MR imaging to assess immediate response to irreversible electroporation for targeted ablation of liver tissues: preclinical feasibility studies in a rodent model. Radiology 2010;256(2):424–432.

26. Guo Y, Zhang Y, Nijm GM, et al. Irreversible electroporation in the liver: contrast-enhanced inversion-recovery MR imaging approaches to differentiate reversibly electroporated penumbra from irreversibly electroporated ablation zones. Radiology 2011;258(2):461–468.

27. Ellis TL, Garcia PA, Rossmeisl JH Jr, Henao-Guerrero N, Robertson J, Davalos RV. Nonthermal irreversible electroporation for intracranial surgical applications: laboratory investigation. J Neurosurg 2011;114(3):681–688.

28. Appelbaum L, Ben-David E, Sosna J, Nissenbaum Y, Goldberg SN. US findings after irreversible electroporation ablation: radiologic-pathologic correlation. Radiology 2012;262(1):117–125.

29. Au JT, Kingham TP, Jun K, et al. Irreversible electroporation ablation of the liver can be detected with ultrasound B-mode and elastography. Surgery 2013;153(6):787–793.

30. Collins JM, Despa F, Lee RC. Structural and functional recovery of electropermeabilized skeletal muscle in-vivo after treatment with surfactant poloxamer 188. Biochim Biophys Acta 2007;1768(5):1238–1246.

31. Park Y, Choi D, Rhim H, et al. Central lower attenuating lesion in the ablation zone on immediate follow-up CT after percutaneous radiofrequency ablation for hepatocellular carcinoma: incidence and clinical significance. Eur J Radiol 2010;75(3):391–396.

32. Rossi S, Di Stasi M, Buscarini E, et al. Percutaneous RF interstitial thermal ablation in the treatment of hepatic cancer. AJR Am J Roentgenol 1996;167(3):759–768.

33. Lewin JS, Connell CF, Duerk JL, et al. Interactive MRI-guided radiofrequency interstitial thermal ablation of abdominal tumors: clinical trial for evaluation of safety and feasibility. J Magn Reson Imaging 1998;8(1):40–47.

34. Clasen S, Pereira PL. Magnetic resonance guidance for radiofrequency ablation of liver tumors. J Magn Reson Imaging 2008;27(2):421–433.

35. Orlacchio A, Bazzocchi G, Pastorelli D, et al. Percutaneous cryoablation of small hepatocellular carcinoma with US guidance and CT monitoring: initial experience. Cardiovasc Intervent Radiol 2008;31(3):587–594.

36. Lee SM, Won JY, Lee DY, et al. Percutaneous cryoablation of small hepatocellular carcinomas using a 17-gauge ultrathin probe. Clin Radiol 2011;66(8):752–759.

37. Silverman SG, Tuncali K, Adams DF, et al. MR imaging-guided percutaneous cryotherapy of liver tumors: initial experience. Radiology 2000;217(3):657–664.

38. Sofocleous CT, Klein KM, Hubbi B, et al. Histopathologic evaluation of tissue extracted on the radiofrequency probe after ablation of liver tumors: preliminary findings. AJR Am J Roentgenol 2004;183(1):209–213.

39. Sofocleous CT, Nascimento RG, Petrovic LM, et al. Histopathologic and immunohistochemical features of tissue adherent to multitined electrodes after RF ablation of liver malignancies can help predict local tumor progression: initial results. Radiology 2008;249(1):364–374.

40. Snoeren N, Huiskens J, Rijken AM, et al. Viable tumor tissue adherent to needle applicators after local ablation: a risk factor for local tumor progression. Ann Surg Oncol 2011;18(13):3702–3710.

41. Sofocleous CT, Garg S, Petrovic LM, et al. Ki-67 is a prognostic biomarker of survival after radiofrequency ablation of liver malignancies. Ann Surg Oncol 2012;19(13):4262–4269.

42. Snoeren N, Jansen MC, Rijken AM, et al. Assessment of viable tumour tissue attached to needle applicators after local ablation of liver tumours. Dig Surg 2009;26(1):56–62.

43. Guo Y, Zhang Y, Jin N, et al. Electroporation-mediated transcatheter arterial chemoembolization in the rabbit VX2 liver tumor model. Invest Radiol 2012;47(2):116–120.